

Phase-dependent space weathering effects and spectroscopic identification of retained helium in a lunar soil grain

K.D. Burgess*, R.M. Stroud

U.S. Naval Research Laboratory, 4555 Overlook Ave. SW, Washington, DC 20375, United States

Received 2 October 2017; accepted in revised form 26 December 2017; available online 3 January 2018

Abstract

The solar wind is an important driver of space weathering on airless bodies. Over time, solar wind exposure alters the physical, chemical, and optical properties of exposed materials and can also impart a significant amount of helium into the surfaces of these bodies. However, common materials on the surface of the Moon, such as glass, crystalline silicates, and oxides, have highly variable responses to solar wind irradiation. We used scanning transmission electron microscopy (STEM) with electron energy loss spectroscopy (EELS) to examine the morphology and chemistry of a single grain of lunar soil that includes silicate glass, chromite and ilmenite, all present and exposed along the same surface. The exposure of the silicate glass and oxides to the same space weathering conditions allows for direct comparisons of the responses of natural materials to the complex lunar surface environment. The silicate glass shows minimal effects of solar wind irradiation, whereas both the chromite and ilmenite exhibit defect-rich rims that currently contain trapped helium. Only the weathered rim in ilmenite is rich in nanophase metallic iron (npFe⁰) and larger vesicles that retain helium at a range of internal pressures. The multiple exposed surfaces of the single grain of ilmenite demonstrate strong crystallographic controls of planar defects and non-spherical npFe⁰. The direct spectroscopic identification of helium in the vesicles and planar defects in the oxides provides additional evidence of the central role of solar wind irradiation in the formation of some common space weathering features.

Published by Elsevier Ltd.

Keywords: Space weathering; Solar wind; Scanning transmission electron microscopy; Ion irradiation; Helium

1. INTRODUCTION

Solar wind irradiation contributes a significant amount of hydrogen and helium to the surfaces of airless bodies and can change optical, chemical, and physical properties of individual rocks and soil grains. The space weathered rims of these grains, as the affected regions are known, are altered significantly by this irradiation as well as other interactions with the space environment, such as micrometeoroid bombardment (Pieters and Noble, 2016). Different materials respond in different ways to irradiation and bombardment, and the altered rims at grain surfaces can include

a variety of features, including amorphous layers, layers of variable composition, nanophase metallic iron inclusions (npFe⁰), and vesicles (e.g., Keller and McKay, 1997). Grains from within the same soil sample can demonstrate significant variability in rim thicknesses and composition (Keller and McKay, 1997), indicating that bulk measurements of the degree of space weathering experienced by a soil do not necessarily reflect the complex processing experienced by the lunar regolith. Recent work on samples returned from asteroid Itokawa show large variations in surface space weathering features on different grains and even different parts of the same grain (Matsumoto et al., 2015, 2016; Noguchi et al., 2014). The grain-to-grain variations can make it challenging to distinguish between the effects of long exposure times, differences in material

* Corresponding author.

E-mail address: kate.burgess@nrl.navy.mil (K.D. Burgess).

properties, and changes in the dominant space weathering process affecting any single grain. Comparisons between individual grains may reflect either different weathering processes or different material responses to the same process.

The presence of helium and other noble gases in space weathered material provides evidence of the influence of the solar wind in altering surface material, but the specific features created by irradiation may not always be distinguishable relative to other processes. For instance, the amorphous rim on a pyroxene grain may differ in composition from the substrate because it is a vapor deposited layer or because the composition was altered due to differential sputtering during irradiation. Some phases allow for more clear discrimination between the various processes, and the Si-free composition of ilmenite, the most common oxide on the lunar surface, means that material that was part of the original substrate can be clearly distinguished from material that was deposited by melt splashes or vapor deposition and that does contain Si (Bernatowicz et al., 1994; Christoffersen et al., 1996). Studying the composition and morphology of ilmenite rims, where solar wind effects can potentially be separated from other processes (Bernatowicz et al., 1994; Christoffersen et al., 1996), and comparing ilmenite to other phases known to have experienced the same exposure conditions can lead to a better understanding of the role of irradiation in creating commonly seen space weathering features.

Helium is ubiquitous in the Solar System, and measurements of its abundance and isotope ratios are important for understanding formation and evolution of many materials. Among common phases present on the Moon, ilmenite is the most retentive of helium (Signer et al., 1977) and highly resistant to amorphization by ion irradiation (Borg et al., 1976). However, the mechanism of trapping and storage of helium in ilmenite and other phases and the conditions of formation of vesicles related to build-up of solar wind implanted material has not been well studied. In addition to lunar samples, implanted solar wind ions have been measured in meteoritic regolith breccias (Suess et al., 1964), micrometeorites and interplanetary dust particles (IDPs) (e.g., Nier and Schlutter, 1992; Kehm et al., 2002; Rajan et al., 1977), and “fossil” micrometeorites in (ancient) deep sea sediments (e.g., Merrihue, 1964; Heck et al., 2004), and used to distinguish presolar or interstellar grains (e.g., Heck et al., 2007; Pepin et al., 2011), but studies of helium abundance have not established how the implanted He is retained, i.e., whether interstitially, in vesicles, or both. Helium is also a key component of the exospheres of the Moon and Mercury (Wieler, 2002), and establishing how or when trapped helium is released from soils could improve our understanding of lifetimes and cycling of exospheric gases.

Characterization of the nano-scale effects of space weathering requires the use of (scanning) transmission electron microscopy (S/TEM) and associated analytical techniques (e.g., Christoffersen et al., 1996; Keller and McKay, 1993, 1997; Noble et al., 2005; Noguchi et al., 2011; Thompson et al., 2016). A number of studies have shown that electron energy loss spectroscopy (EELS) in a

S/TEM is a valuable technique for identifying and measuring the helium in nano-scale cavities in a number of materials, including laboratory irradiated metals and semiconductors (e.g., David et al., 2014; Fréhard et al., 2009; Walsh et al., 2000) and radiogenic minerals (Seydoux-Guillaume et al., 2016). Spectroscopic signatures of hydrogen in vesicles in the space weathered rim of a pyroxene grain from an IDP were identified using this technique (Bradley et al., 2014). In the present study, we were able to examine a lunar soil grain in which silicate glass, chromite, and ilmenite are exposed along the same surface. The sections were prepared for analysis in the STEM using a focused ion beam microscope (FIB), which leads to sections in which multiple space-exposed edges of a single grain can be viewed. Results shown here show a range of space weathering features in the three exposed phases, including crystallographic orientation effects in the ilmenite. The EELS data show conclusively the presence of helium in vesicles in the space weathered rim of the ilmenite and in small defects in both the ilmenite and chromite.

2. MATERIALS AND METHODS

The soil grain examined here is from sub-mature soil 71501,288. The soil has been previously characterized by the Lunar Soil Characterization Consortium (LSCC) (Taylor et al., 2001) and in a number of bulk, mineral separates, and single grain noble gas analyses (Becker and Pepin, 1989; Nier and Schlutter, 1994; Benkert et al., 1993; Heber et al., 2003; Nichols et al., 1994; Pepin et al., 1999). Exposure ages and crater counts for the collection region group around 100 Ma and are linked to secondary impacts associated with Tycho crater (Arvidson et al., 1976). Plagioclase grains from this soil have an average of 6.7×10^8 tracks/cm² for 68 individual grains (Wieler et al., 1980), which gives an exposure age of ~15 kyr (Berger and Keller, 2015).

A small amount of the soil was dispersed on a sticky carbon substrate, coated with a thin layer of carbon, and examined in a scanning electron microscope (SEM). The grain described here is an ilmenite dendrite crystal, with silicate glass and quench crystals filling regions between ilmenite limbs (Fig. 1). Thin chromite lamellae are inter-grown with the ilmenite in some areas, and all three phases are exposed at the original surface of the grain. Two sections from the grain were prepared by focused ion beam microscopy (FIB) with a FEI Nova 600 FIB-SEM. Regions of interest on the grain were coated with a thick ion beam deposited carbon film (1–2 μm) over a thin layer of evaporated carbon before ion milling to prevent damage to the grain surface by the ion beam. A Ga⁺ ion beam voltage of 30 kV and variable probe current was used for sectioning. Both the top and bottom space-exposed surfaces of the original grain are visible in section 1 (Fig. 1b), with a layer of the carbon tape substrate attached to the bottom surface, while only the bottom surface of section 2 was maintained intact after thinning (Fig. 1c). The sections were attached to a Cu half-grid using a Pt weld and thinned to electron transparency; final thinning was done at 30 kV, 40 pA. The final thickness was calculated to be ~130 and

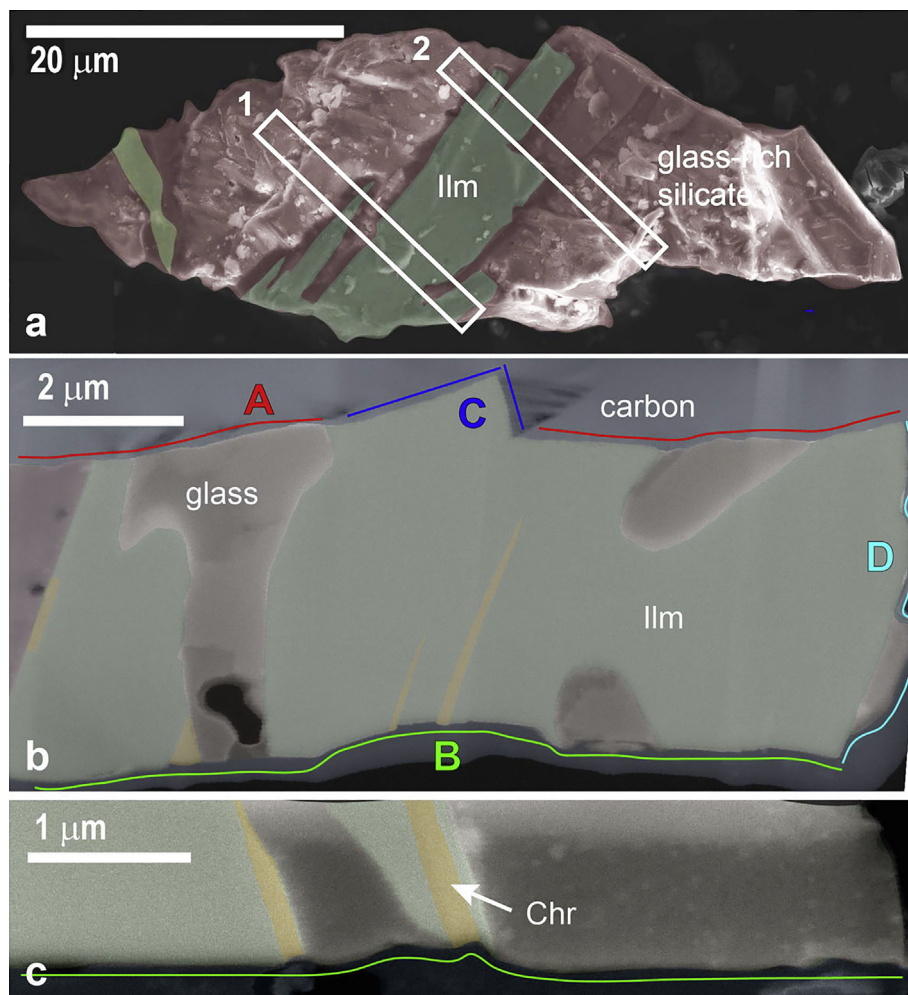


Fig. 1. (a) False color secondary electron (SE) image of the lunar soil grain prior to FIB preparation. Areas of silicate glass are shaded red, ilmenite is green, and chromite is yellow. Two FIB sections were extracted from the grain from the highlighted regions. (b, c) SE images of section 1 and section 2, respectively. The space-exposed surfaces of the sections are labelled A, B, C, or D according to space weathering features and crystallographic orientation. All four regions are present in section 1 while section 2 includes only region B.

~150 nm for the two sections based on the mean free path of ilmenite (Egerton, 2011). This is slightly thicker than optimal for most EELS applications, but this allowed for more nanobubbles to be retained in the sections, unaffected by the FIB preparation, and had only a small effect on the energy loss range of interest for the study of helium. The extracted sections were stored in a desiccator and baked under vacuum at 140 °C for 8 h to drive off adsorbed water for analysis in the ultra-high vacuum microscope. The bake-out temperature is ~30 °C above the maximum day-time temperature at the Apollo 17 site (Keihm and Langseth Jr., 1973). The sections were analyzed on several different occasions, the first being immediately following FIB preparation, and measurements were compared in each case to ensure the sample was not altered by the bake-out process. Chemistry, iron oxidation state, and helium peak intensity did not change across repeated measurements or microscope sessions.

2.1. STEM measurements

The FIB sections were imaged using a JEOL 2200FS and NION UltraSTEM-X at the U.S. Naval Research Laboratory. STEM images were collected in bright field (BF) mode and high-angle annular dark field (HAADF) mode, which is sensitive to atomic number and thickness differences. Electron energy loss spectroscopy (EELS) and energy dispersive X-ray spectroscopy (EDS) data were collected with the UltraSTEM-X, which is equipped with a Gatan Enfium ER EEL spectrometer and a windowless, 0.7 sr Bruker SDD-EDS detector. The STEM was operated at 200 kV and ~40 pA, with a 0.1 to 0.2 nm probe. Data for EELS and EDS were collected as spectrum images (SI), with a spectrum collected for each pixel to map variations in thickness and composition. The energy dispersion for EELS measurements was 0.02 or 0.05 eV/channel with an energy resolution, calculated from the zero-loss peak

(ZLP) FWHM, of 0.36 or 0.45 eV, respectively. Peak alignment to compensate for energy drift during EELS SI acquisition was carried out using Gatan Digital Micrograph software. A Fourier-log deconvolution was performed on each spectrum image to account for plural scattering and thickness changes. For EDS data collection, the beam was scanned at a rate of 16 $\mu\text{s}/\text{pixel}$ for 100–300 frames. Semi-quantitative maps were calculated using the Cliff-Lorimer method with default k -factors. Linear defects in the ilmenite were traced by eye in HAADF images, and lengths and areal density of defects and areas of cavities were calculated using ImageJ software.

2.2. Quantification of helium

The helium K-edge ($1s \rightarrow 2p$ transition) is at ~ 22 eV in EELS, which is on or between the silica plasmon peak energy (~ 22 eV) and the peak energy of the ilmenite and chromite plasmons (~ 25 eV). The energy of the He peak increases with increasing pressure or density of trapped helium (Jäger et al., 1982) and can vary by up to ~ 3 eV. The density of helium trapped in vesicles or cavities in the ilmenite was calculated following the method of Walsh et al. (2000). When possible, the plasmon background was removed by subtraction of the bubble rim spectrum from the spectrum showing the helium peak. Where this was not viable due to the bubble spectrum having significant background contributions from both ilmenite and an amorphous silica-rich rim, the background was removed in one or two steps with a second-order polynomial function and a linear function. A Gaussian was fit to the helium peak (Supplementary Material S1). Helium concentration within each bubble is calculated from

$$n_{\text{He}} = \frac{I_{\text{He}}}{\sigma d I_{\text{ZLP}}} \quad (1)$$

where n_{He} is the number of helium atoms per nm^3 , I_{He} is the integral of the helium peak after removal of the background and fitting as described above, I_{ZLP} is the integral of the zero-loss peak, σ is the helium cross-section at our microscope parameters, and d is the bubble thickness calculated from the relative thickness t/λ using the mean free path λ for helium (Egerton, 2011). Two different methods for calculating σ provide values that vary by $\sim 25\%$ (Egerton, 2011; Walsh et al., 2000), contributing systematically to the error in the density calculation. Bubble thickness is calculated relative to the thickness of the surrounding material, and can thus be affected by the presence of npFe^0 and the amorphous silicate layer compared to ilmenite. The resulting concentration is sensitive to the thickness measurement, which can vary significantly pixel by pixel.

3. RESULTS

Section 1 captures three “faces” of the grain that have been divided into four regions based on visible space weathering features in the ilmenite and the crystallographic orientation of the exposed surface. The four regions are noted in Fig. 1b, and details of the categorization are provided in

Section 3.1.3. Section 2 includes only the portion of the grain in region B (Fig. 1c). (The location of each image shown below within the sections is shown in Supplementary Material S2.) Gallium from the FIB preparation is seen only in the carbon layer coating the top surface of section 1 (region A), which was ion-deposited. The lack of Ga in the silicate or oxides in EDS measurements indicates that the differences between regions A and B cannot be attributed to damage during section preparation.

3.1. Space weathering morphology

3.1.1. Silicate glass

Of the three phases exposed to space weathering in the soil particle, the glass-rich silicate shows the least evidence of alteration. Fig. 2 shows a region of the silicate glass and quench crystals exposed near both chromite and ilmenite. The bulk glassy region has an average composition of ~ 53 wt% SiO_2 , ~ 32 wt% Al_2O_3 , ~ 8 wt% CaO , and 1–3 wt% each of MgO , FeO , Na_2O and TiO_2 but varies locally due to the quench crystals, which can be seen as the brighter and darker areas within the glass. Most of the silicate material is amorphous, meaning any solar wind irradiated layer in which the structure was altered by implanted ions may not be readily apparent. However, most near-surface quench crystals within the glass do not appear altered.

In addition to the general lack of clear altered rim, there is also no evidence of vesicle formation within the glass, and npFe^0 inclusions are limited to very thin, discontinuous layers or to restricted regions near Fe-rich quench crystals. In Fig. 2, the npFe^0 inclusions coating the silicate region appear to be in an Mg-rich amorphous layer over Mg-rich quench crystals; it is unclear if the layer is vapor deposited or damaged by ion implantation. The EDS data from the space-exposed silicate surface show no systematic variations in composition with depth, as might be expected due to differential sputtering (e.g., Keller and McKay, 1997). Fig. 3 highlights a portion of the silicate matrix with a relatively large pyroxene crystal at the surface. The npFe^0 inclusions are seen only in a thin layer very near the crystal and are not present elsewhere in the glass, which is Fe-poor here. The region rich in very small (< 4 nm) npFe^0 inclusions is thin, with a maximum of ~ 40 nm depth, but most of it is < 25 nm. The sulfides here are crystallized from the melt and not associated with any space weathering process. Sulfide grains up to a few hundred nanometers across are observed at several ilmenite-glass interfaces and smaller inclusions are seen on or near pyroxene grains, as in Fig. 3.

No solar flare tracks were noted in the pyroxene or other silicate quench crystals. The largest quench crystal in these sections has an area of $\sim 1 \mu\text{m}^2$ and could be expected to have between 1 and 10 tracks, based on the range of solar flare track densities observed in plagioclase grains from this soil (Wieler et al., 1980). Our lack of observation of tracks indicates the grain likely received a radiation dose at the low end of the range for this soil, but some is somewhat constrained by the total area observed under BF STEM conditions.

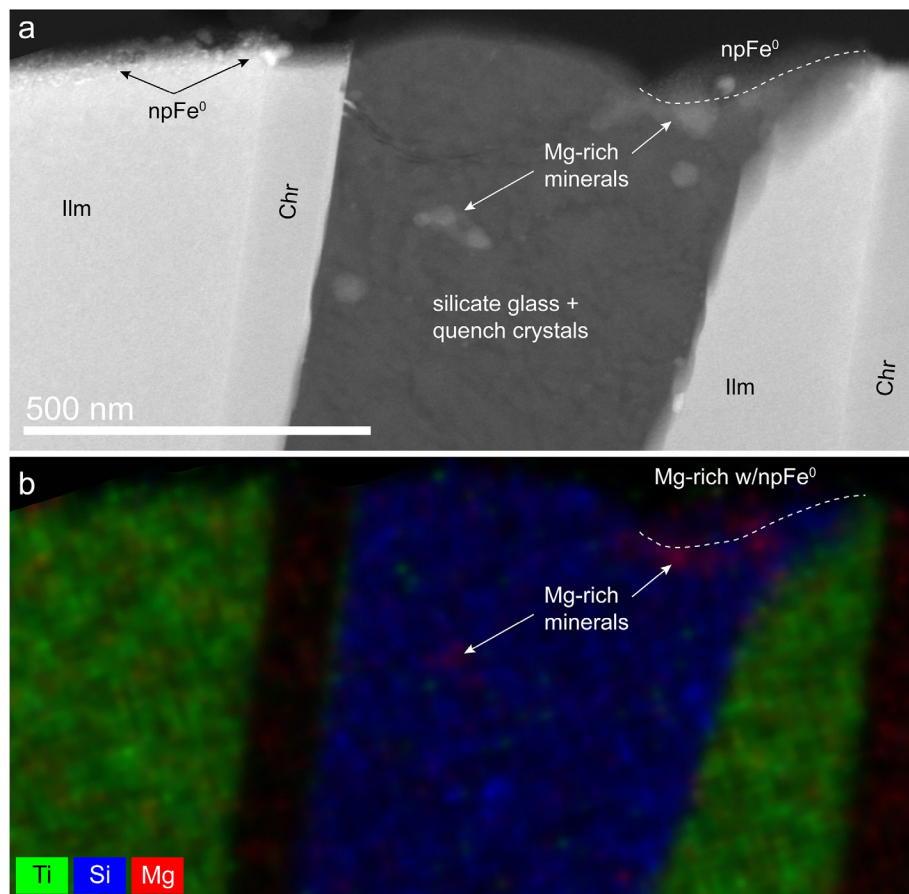


Fig. 2. (a) HAADF image and (b) semi-quantitative EDS element map from section 2 showing a surface exposing ilmenite, chromite, and glassy silicate with quench crystals. The brighter phases within the glassy region have higher Mg and Fe. The ilmenite to the left has a distinct rim rich in defects and npFe⁰. The rim of the chromite is also disordered and defect rich, but it lacks vesicles and npFe⁰ other than a single large particle on the very surface. Much of the silicate region lacks an obvious rim, but a portion of the surface to the right side is coated by <3 nm npFe⁰ in material richer in Mg than surrounding matrix with a single larger Fe-rich particle. The dotted line traces the boundary between the unaltered silicate and the npFe⁰-rich layer. The location of this image in context of the larger sample is shown in S2.

3.1.2. Chromite

In this grain, aluminian-chromite (hereafter, chromite) is inter-grown with the ilmenite with (111)_{cr} parallel to (001)_{ilm}. At least four thin lamellae (50–150 nm) were seen in the ilmenite both relatively near and far from glassy regions (Fig. 1b and c). In some but not all surface exposures of the chromite-ilmenite interface, a ~50 nm step is present between the two phases (Fig. 4a), but either phase may be the one in higher relief. A thicker curtain of amorphous Si-rich material is often seen in the corner formed at the phase interface (Fig. 4b and c). Thin planar cavities are also often seen along the interface between the phases near the grain surface.

The exposed surface of the chromite is crystalline, but defect-rich, to a depth of ~65 nm (Fig. 4). In general, the defects and small cavities are sub-parallel to the exposed surface and slightly curved rather than falling along a specific crystallographic plane, which is highly distinct from the alignment of defects in the ilmenite (Section 3.1.3). The EELS measurements show that helium is present in some

of the defects (Fig. 4d). Nanophase iron-rich inclusions are rarely present in the rim of the chromite except in a thin layer at the very surface that is rich in other vapor deposited elements such as Si (Fig. 4e). Fig. 2 also shows a distinct lack of npFe⁰ inclusions in the chromite compared to the ilmenite, with the exception of a couple of larger than average Fe-rich grains attached to the surface. Where a few npFe⁰ inclusions appear to be in the chromite itself in addition to along the surface (Fig. 4b), they are <3 nm in diameter, significantly smaller than inclusions in nearby ilmenite (6–15 nm).

3.1.3. Ilmenite

Most of the two sections extracted from the grain are composed of ilmenite, and the four categories used to delineate the regions of exposure (Fig. 1b and c) are based on weathering features noted in the ilmenite. All surfaces of the original grain seen in the sections have been exposed to varying degrees of space weathering and can be classified based on the angle between the space weathered surface and the (001) plane in ilmenite and the average size of recogniz-

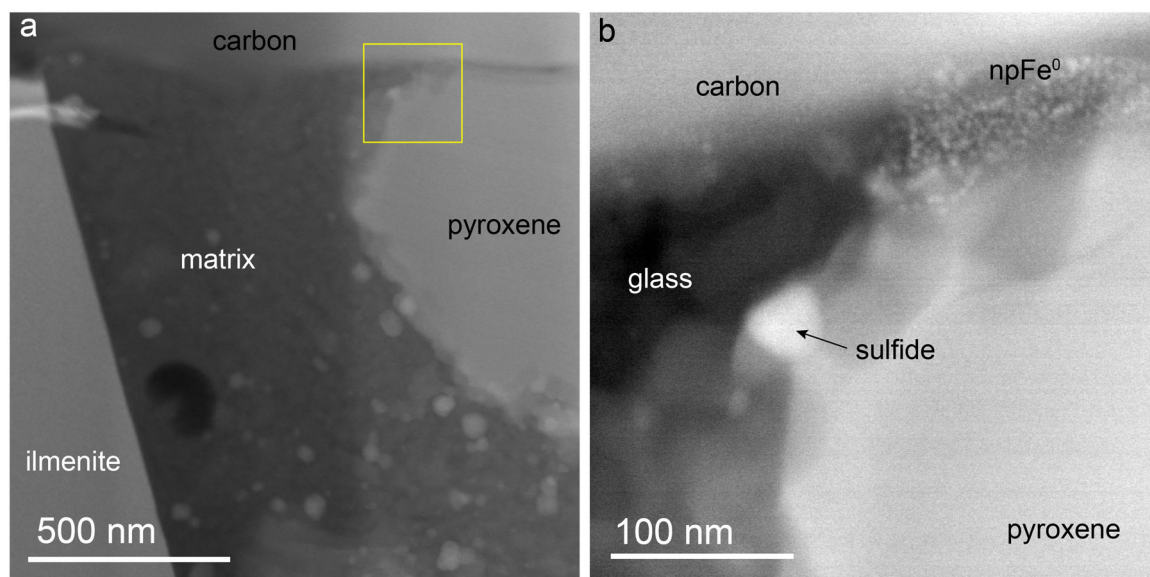


Fig. 3. (a) HAADF image of a portion of section 1, region A where ilmenite is adjacent to glassy silicate on the exposed surface. (b) Higher magnification view of the area indicated in (a). Small sulfide and silicate quench crystals are present in the glassy matrix, as well as a larger pyroxene crystal. The glassy iron-poor region of the glass lacks an obvious rim, and quench crystals are present to the grain surface. However, <4 nm npFe^0 inclusions are present where the pyroxene grain is near the surface.

able vesicles (Fig. 5). Significant differences are seen in defect areal density and vesicle number in different regions. Regions A and B are on opposing sides of the section, and both are close to perpendicular to $(001)_{\text{ilm}}$. However, the vesicles in region A are on average much larger and somewhat rounder than those in region B. Region C has a surface $\sim 40^\circ$ from the basal plane and large vesicles, and region D ranges from almost parallel to the basal plane to $\sim 40^\circ$ but lacks the large vesicles.

The ilmenite space weathered rim is partially crystalline and is generally comprised of several layers, in agreement with Christoffersen et al. (1996). (A schematic representation of the layers is included in Supplementary Material.) From the grain interior to the space-exposed surface, the ilmenite contains: (1) undamaged substrate material; (2) a layer of thin, crystallographically oriented defects (inner rim); (3) a defect-rich, nano-crystalline layer rich in npFe^0 that may contain larger vesicles (outer rim); and (4) a discontinuous Si-rich vapor deposited layer of variable thickness with abundant in <5 nm npFe^0 (vapor rim).

3.1.3.1. Inner rim. The parallel, planar defects on all sides of the ilmenite grain extend in the ilmenite to a depth of ~ 70 – 100 nm regardless of the orientation and areal density of the defects (Fig. 5). In both HAADF and EDS, the planar defects, which are the width of one unit cell, are noted only by changes in intensity with no major element compositional changes relative to surrounding material, indicating they are cavities in the ilmenite. The EELS data show evidence of helium in a few of the defects (Fig. 6). The ilmenite itself is sometimes slightly depleted in Fe in this near-surface region relative to bulk, undamaged ilmenite, as seen in EELS data from this layer (Fig. 7). Changes in EELS Ti

L-edge peaks in this layer are consistent with slight reduction of the Ti valence state toward the space-exposed surface (Zhang and Keller, 2010; Christoffersen et al., 2010; Keller et al., 1995).

In one location in region A, a group of planar features aligned with $(001)_{\text{ilm}}$ are present near the ilmenite surface (Fig. 7). These defects are wider and longer than the other aligned defects, although similarly oriented within the ilmenite. Both EDS and EELS data show that the large defects are filled with TiO_2 , as opposed to helium. The small, narrow (He-filled) defects are also present in this area, just below a layer rich in Si and depleted in Fe. A large metallic Fe grain fills a portion of the crack just below the TiO_2 -filled defects.

3.1.3.2. Outer rim. Within the top 35–40 nm, the ilmenite is mostly crystalline but disordered and rich in npFe^0 , with distinct differences in npFe^0 size, shape, and abundance between regions. The npFe^0 inclusions are generally larger in C and D by about a factor of two, and the inclusions in A are rounder, especially where they are present in the thin Si-rich layer. In regions B, C and D, vesicles are seen only in the npFe^0 -rich layer, while in A, some vesicles extend into the thin Si-rich layer coating the ilmenite. As described in Section 3.2, helium was measured in some of these vesicles. Fig. 8 shows a portion of region B with several helium-containing vesicles in the disordered rim that are not all obvious in the HAADF image but can be mapped out using a window mapping routine. Region B in general has fewer vesicles than other regions, and it also has surfaces where there is no disordered, npFe^0 -rich layer, and the aligned defects extend to the surface from a depth of ~ 90 nm (Fig. 5b). In section 1, a large crack formed

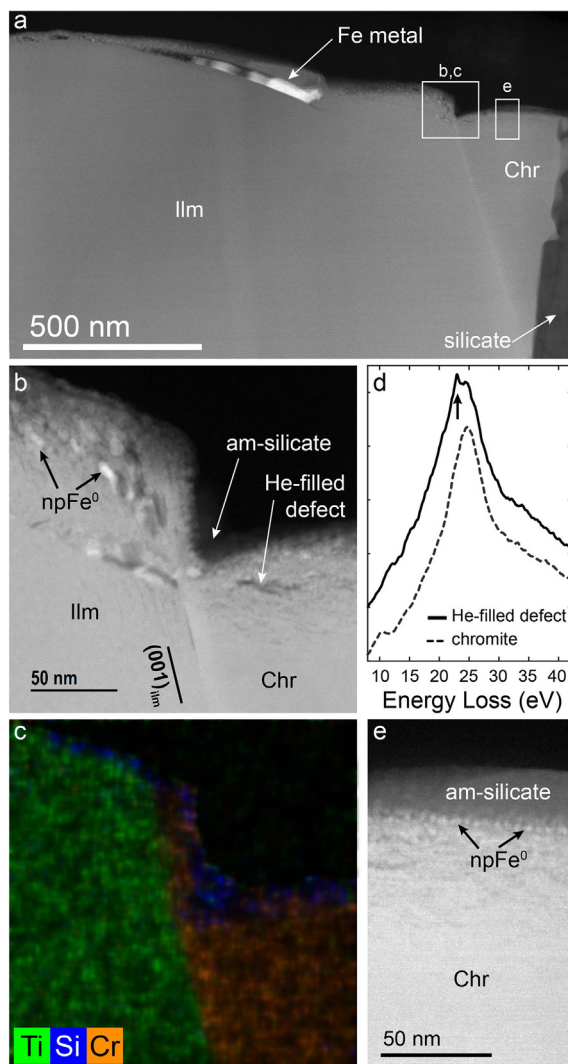


Fig. 4. (a) HAADF image from section 1, region B showing a crack sub-parallel to the ilmenite surface and partially filled by metallic Fe grains. Steps in the surface are present at the end of the crack and at the interface between the ilmenite and chromite. The ilmenite rim contains several vesicles, and the chromite is partially coated by an amorphous silicate layer. (b) HAADF image of ilmenite-chromite interface and space weathering features. The chromite contains curving, irregular defects extending to ~ 65 nm depth. The ilmenite contains aligned, planar defects and larger npFe^0 inclusions within the disordered layer. (c) Semi-quantitative EDS element map of region in (b) showing the build-up of Si-rich material in the corner created by the ilmenite-chromite boundary. (d) Selected EELS data from the region show the presence of a small amount of helium within some of the defects (~ 22 eV). (e) HAADF image of defect-rich chromite rim coated by npFe^0 in a thin band and amorphous Si-rich material.

sub-parallel to the surface across a portion of region B and filled with metallic Fe grains (Fig. 4a). Helium was measured inside the crack.

3.1.4. Vapor rim

A thin, amorphous, Si-rich layer covers portions of the ilmenite, chromite, and glass. On the ilmenite, the layer coats the disordered layer, particularly in regions A and

C. In one location the Si-rich coating reaches a thickness of ~ 70 nm, but the thick portion is only ~ 330 nm across. Ubiquitous npFe^0 inclusions ~ 5 – 7 nm in diameter are present in the coating, and the ilmenite under the thickest portion contains aligned defects but not to as great a depth as in uncoated areas. Most of the Si-rich layer is much thinner than 20 nm, although it is everywhere full of ~ 5 nm npFe^0 inclusions. Al and Ca are present in the vapor deposited layer coating ilmenite, and Fe/Si and Mg/Si are consistently higher in vapor deposited material coating glassy regions than in the bulk glass. However, the layer in most places is too thin to obtain a reliable composition that is not significantly influenced by the beam interaction with the substrate phase. Where vapor deposited layers extend across both the glassy region and the ilmenite, Al/Si and Ca/Si are greater in the coating on the silicate portion than on the ilmenite directly adjacent (and elevated relative to the bulk silicate composition). However, the ratios are not necessarily higher than in coatings elsewhere on the ilmenite. At the sharp corners formed between chromite and ilmenite, a thicker curtain of amorphous Si-rich material is often seen (Fig. 4b and c).

3.2. Helium implanted in space weathered rims

The abundance of helium was measured in 13 different bubbles (vesicles still containing helium) in the four regions of the ilmenite (Supplementary Material Table S1). Vesicles that do not contain helium were likely cut or perforated by the ion beam during sample preparation. The concentration of helium ranges from 20–130 He/nm^3 and peak energies range from 22.1 eV to 24.3 eV (Fig. 9a). In some cases, bubbles that are within a few 10s of nanometers of each other exhibit a large range in peak energy and helium concentration (Fig. 9b). The helium peak from bubbles in regions C and D is shifted to generally higher values than in A and B, indicating higher pressure and higher helium density. As noted above, helium was also observed in defects in both the ilmenite and the chromite, but the area of a single defect is small and the helium is close to the detection limit. Errors associated with attempts to calculate the helium concentration in the planar defects are large. Multiple scans of the same bubble do not cause any change in peak energy or intensity, as has been seen in some materials (David et al., 2014). However, abrupt loss of the helium signal was seen after a stationary beam dwelled on a bubble for several seconds and perforated its surface.

Crystallographic orientation does not appear to play a role in vesicle depth, although it does play a limited role in their shape. The vesicles are predominantly observed in the disordered layer of the ilmenite rim, and the depths correlate well with expected implantation depths of helium from the solar wind (Christoffersen et al., 1996). Many small vesicles are intimately associated with elongated npFe^0 and are also aligned with the basal plane in regions C and D, indicating a continuum between the defects in the interior rim and the larger vesicles in the outer rim (Fig. 5d).

Hydrogen, more abundant than helium in the solar wind, was not clearly detected in the sample or any of the

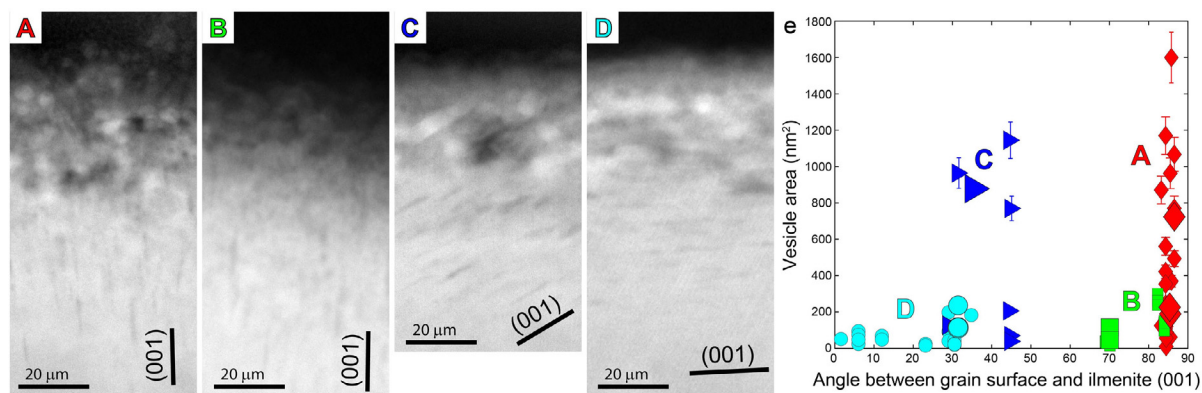


Fig. 5. (a-d) HAADF images showing characteristics from the four regions of the ilmenite surface. Images have been rotated to show solar wind direction from the top, but are from the sides of the sections as noted in Fig. 1. The four regions have different relationships between the crystal lattice and exposed surface, which is clearly expressed in the alignment of the planar defects. Vesicles appear as dark regions within the disordered layer, and npFe^0 are bright. (e) Plot showing the relationship between ilmenite (001) and vesicle size in the different regions. Larger symbols indicate the vesicles in which helium was measured in this study. The locations of the images in context of the larger sample are shown in S2.

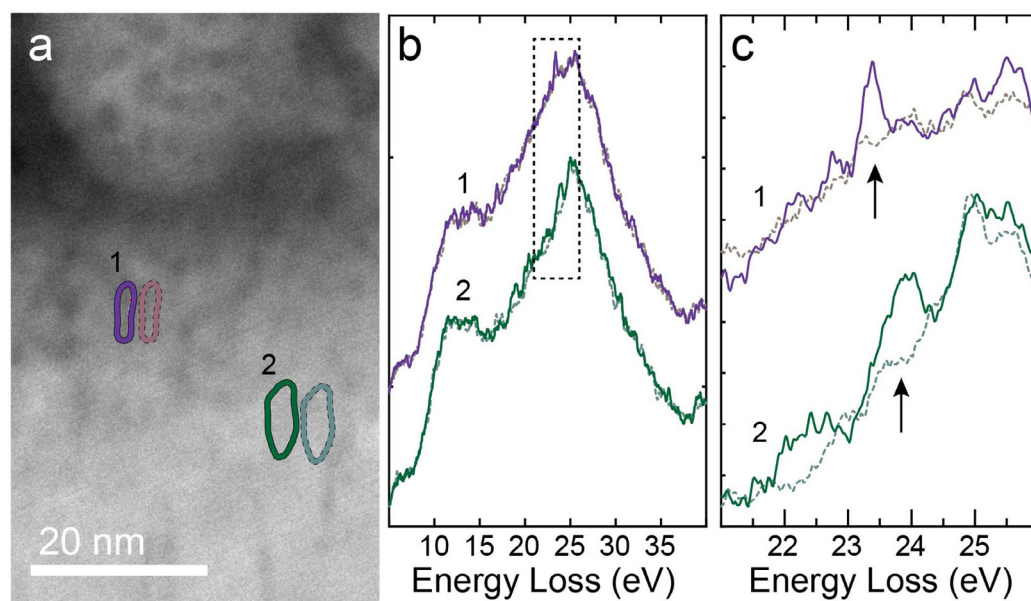


Fig. 6. (a) HAADF image from a portion of section 1, region A showing aligned defects near the exposed surface and a pitted npFe^0 particle. (b) EELS spectra from two defects ~ 5 nm long showing the presence of small peaks near 23 eV, indicating the presence of helium. Spectra from directly next to the defects are shown for comparison (dashed lines). (c) Closer view of EELS data shows helium peaks do not appear in ilmenite directly next to the defects and are distinct from noise.

bubbles. The H K-edge is at ~ 13 eV, and this peak as well as several other lower energy peaks associated with water has been observed in EELS spectra of vesicles in an IDP pyroxene and in experimentally irradiated samples (Bradley et al., 2014). However, ilmenite, like other Ti^{4+} -bearing phases such as rutile, has a small peak at ~ 13 eV. Spectra in Fig. 7b show no significant difference between bubble and ilmenite matrix in the 13 eV region, but a large peak is present in the TiO_2 at that energy (also seen in TiO_2 standard material). The exposed silicate regions in this grain contained no vesicles, and also showed no evidence of hydrogen.

4. DISCUSSION

4.1. Space weathering in ilmenite, chromite and glass

The various processes that cause space weathering can occur on a number of timescales, and their effects are influenced by many factors, including material, temperature, magnetic fields, and location in the Solar System (Pieters and Noble, 2016). The presence of multiple phases in the same grain, adjacent to each other, as well as multiple sides of the grain being observed in context, provides a way to begin to unravel the effects of material and crystallographic

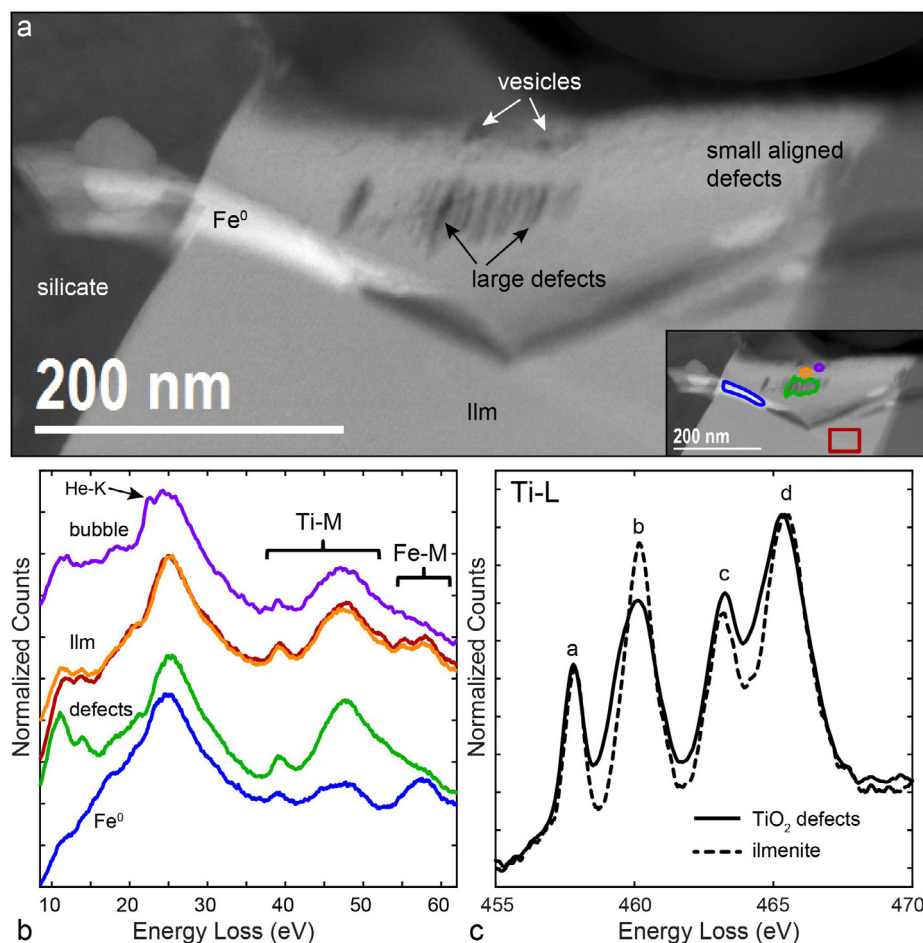


Fig. 7. (a) HAADF image of a portion of the ilmenite in section 1, region A that contains large aligned defects. Smaller defects similar to those seen in other regions of the ilmenite are seen closer to the surface, as are several vesicles. The inset shows the regions from which EELS data shown in (b) and (c) were summed. (b) Low-loss EELS data show significant differences between the large defects (green) and the surrounding ilmenite (red, orange), as well as the presence of helium in small defects closer to the surface in a layer that lacks Fe (purple). A large Fe metal grain is present in the crack (blue). The peak at ~ 13 eV in the TiO₂ is also seen in lab grown TiO₂ and is not related to H irradiation. Spectra are offset vertically for clarity. (c) Ti L-edge data from the large Ti-rich defects (solid) and unaltered ilmenite (dashed). Differences in the relative height of the four characteristic peaks indicate that these defects are filled with TiO₂. (For interpretation of the references to colour in this figure legend, the reader is referred to the web version of this article.)

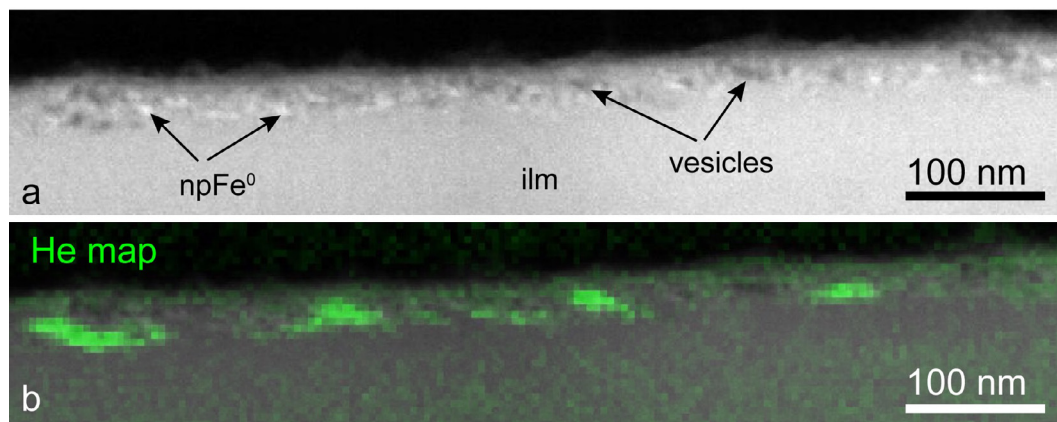


Fig. 8. (a) HAADF image of a portion of section 2, region B showing the npFe⁰-rich disordered rim. (b) Overlaid on the image is a map of the helium peak in green. Several bubbles are present within the rim.

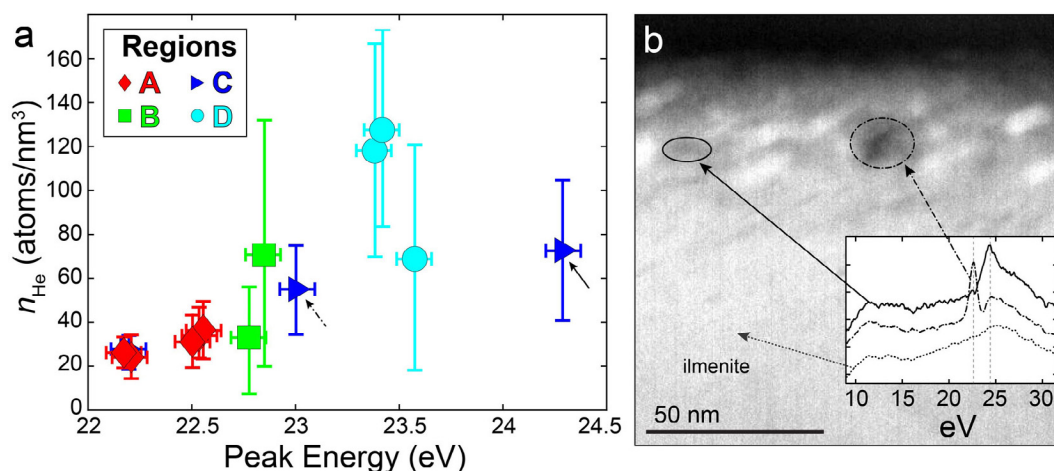


Fig. 9. (a) Plot of helium K-edge peak energy versus the calculated density of helium based on peak intensity for 13 vesicles with measured helium. Bubbles in regions A, B, C and D are shown as diamonds, squares, triangles, and circles, respectively. The much larger interior pressure in bubbles in region C relative to A is evidence of the influence of crystallographic orientation of the ilmenite, as they regions are on the same side of the grain. Helium content was also measured in several planar defects, but uncertainty in the thickness measurement contributes to large error in the concentration estimate. (b) HAADF image of a portion of the ilmenite rim from region C. Inset EELS spectra are from two bubbles separated by ~ 50 nm that have very different peak energies (solid, dashed). A spectrum from ilmenite with no vesicle (dot) is shown for comparison. Spectra are offset vertically for clarity. Data points in (a) for these two bubbles are indicated by the arrows.

orientation from differences in exposure history. Individually, the phases appear to represent different degrees of space weathering: the silicate has little space weathered rim to speak of and appears to have very limited exposure; the chromite has a well-developed rim but only a small amount of npFe⁰; and the ilmenite appears to have undergone significant irradiation exposure, having a well-developed rim, abundant npFe⁰, and relatively large, helium-filled vesicles. Together, however, the phases illustrate the variability that can occur over very short length scales within a single soil grain and the extent to which nano-scale features associated with space weathering depend on substrate phase.

4.1.1. Vapor deposition

A vapor deposited rim is a common feature observed on space weathered material from the Moon and Itokawa. The hallmarks of such a rim include an amorphous structure, a composition rich in Si that does not match the substrate composition, and in many cases the presence of layers of small (<5 nm) npFe⁰ inclusions (Keller and McKay, 1997; Pieters et al., 2000). The vapor deposited material on this grain forms very thin, discontinuous layers, clearly distinguishable by the presence of Si coating ilmenite and chromite in some regions. A very thin layer rich in npFe⁰ is also present along portions of the silicate and chromite surface where no other npFe⁰ are seen at depth within the sample.

Where it is present, the composition and thickness of the layer changes across the phase interfaces, indicating that the substrate phase affects deposition rates and resputtering of deposited material. Ilmenite is more resistant to sputtering than both amorphous and crystalline silicates (Borg et al., 1976), and as such, any silicate deposition layer that does form could be affected by sputtering enhanced by corners and sharp edges on the ilmenite. Sharp corners are

also seen at grain boundaries between ilmenite and chromite that tend to be filled by thicker Si-rich layers than in other areas. Additionally, sputter yield amplification, due to the high density and high average atomic number of ilmenite compared to silicates on the Moon (Berg and Katardjiev, 1999), may enhance the differential sputter rates among specific ions already seen within the irradiated layer of many grains (e.g., Carrez et al., 2002). This could lead to both differences in composition of the vapor deposited layer over small length scales, which could in turn affect the presence and density of npFe⁰ inclusions, and to continuing alteration of the layer after it is deposited.

Sputtering due to ion irradiation and micrometeoroid bombardment could both produce vapor deposits (Hapke, 2001; Sasaki et al., 2001). However, the variations in composition and thickness of the vapor deposited layer over very short length scales indicate that the processes are complex and cannot be easily separated on lunar samples. Samples from Itokawa, where space weathering is hypothesized to be much more strongly influenced by solar wind irradiation relative to impacts compared to on the Moon, have relatively thin vapor deposited rims (Harries and Langenhorst, 2014; Matsumoto et al., 2015; Noguchi et al., 2014, 2011; Thompson et al., 2014), similar to what is observed on our sample. This could suggest a primary role of sputtering in the formation of vapor deposited rims that are consistently very thin. In the future, comparisons with experimental work may allow us to understand possible compositional trends characteristic of specific processes, but at present, detailed data that take into account the initial phase, the substrate phase, and the effects of further irradiation and sputtering do not exist.

4.1.2. Irradiated material

Most of the damaged rim formation in the ilmenite and chromite is attributable to solar wind irradiation and ion

implantation. Chromite and ilmenite both retain measurable amounts of helium in their irradiation-damaged rims and contain elongated defects aligned sub-parallel to the irradiated surface in chromite or the (001) plane in ilmenite. The shape and alignment of defects within the two materials are consistent with experimental helium irradiation of spinel (MgAl_2O_4) and corundum (Al_2O_3), which have analogous structures to chromite and ilmenite, respectively, under a variety of conditions (Zinkle, 2012). In the silicate, a few pockets of npFe^0 inclusions, such as that shown in Fig. 3, are the only indication of this irradiation. Even there, the inclusions are present only where pyroxene was the space-exposed phase. The glassy nature of most of the silicate in these sections could make the effects of ion irradiation difficult to identify, but even so, most near-surface quench crystals within the glass do not appear altered, and no compositional variations near the surface of the glass were observed, as might be expected after significant irradiation (Keller and McKay, 1997; Carrez et al., 2002). The lack of observed solar flare tracks is also consistent with the low degree of exposure inferred from a thin to absent rim in the silicate (Zhang and Keller, 2011), but this is in distinct contrast to the well-developed irradiated rims in the oxide phases. Conditions for helium saturation are reached too quickly (<1000 years) for vesicle formation to inform exposure time-scales (Nichols et al., 1994).

The apparent differences in maturity between the three main phases, that is, the lack of damaged rim in the silicate region, the defect-rich rim in chromite, and the complex npFe^0 -, defect- and vesicle-rich rim in ilmenite, all produced in the same exposure environment, were not necessarily expected based on previous experimental results. For example, the ion doses required for significant bubble nucleation and growth in many oxides and metals are on the same order as that needed to achieve amorphization and vesicle formation in most silicates (e.g., Carrez et al., 2002; Christoffersen et al., 2010; Christoffersen and Keller, 2011; Zinkle, 2012). This indicates that conditions in the natural environment that are not accounted for in most experiments aimed at replicating solar wind irradiations, such as dose rate, temperature during irradiation, mix of ion types, and compositional variations in the substrate (Rice and Zinkle, 1998; Carter and Nobes, 2011; Zinkle, 2012; Hobbs et al., 1994), could play a significant role in material response at the lunar surface. While it is known that increasing flux or decreasing temperature at the same total dose can lead to an increase in the amount of amorphous material (Carter and Nobes, 2011), the effect of such changes on npFe^0 production has not been studied experimentally.

The differences in conditions between experiments and the natural environment, and the morphological changes related to such differences, could affect interpretations of exposure history of different airless bodies, which do not all experience the same temperature and flux conditions (Bennett et al., 2013). On the Moon, decreased flux of solar wind ions is hypothesized to be the cause of lunar swirls (Glotch et al., 2015) and latitudinal variations in spectral features (Hemingway et al., 2015). The differences in material response to irradiation at high experimental fluxes and

the lower flux at the lunar surface could be exacerbated at even lower fluxes in swirls and at the lunar poles. In these conditions, even slight variations in modal abundances of phases exposed to the space environment could have significant effects on remotely sensed data.

4.1.3. Nanophase metallic iron

Three “types” of metallic iron inclusions were noted in this grain: <5 nm spherical inclusions generally associated with vapor deposited layers, 10–50 nm spherical and elongate inclusions in the disordered layer of the ilmenite rim, and large (>100 nm) grains associated with cracks near the rim of the ilmenite. Iron-rich inclusions within the glassy silicate matrix are predominantly sulfides, but they are related to melt processes rather than space weathering. The abundance of npFe^0 inclusions in and on the silicate portions of the grain appears highly influenced by the composition of the quench crystals (pyroxene) near the surface, as in both Figs. 2 and 3 where the substrate contains relatively more Mg and Fe compared to most of the silicate. The chromite, although containing significant Fe and having a defect-rich rim, has very few npFe^0 inclusions, and most are directly on the surface and coated by amorphous silicate, as in Fig. 4. By contrast, the disordered rim of the ilmenite is rich in npFe^0 . Many of these inclusions are associated with cavities, and the size and shape of the defects could influence npFe^0 formation and growth (or vice versa). Fig. 9b shows some inclusions elongate in the same direction as the aligned defects in the inner rim of the ilmenite.

The metallic grains present in the cracks in the ilmenite are too large to be considered npFe^0 by most definitions that restrict nanophase to indicate inclusions likely to cause reddening of the visible to near-IR wavelength range rather than darkening (Pieters and Noble, 2016). However, most work on the effects of small optically active opaque grains have assumed spherical shapes (Lucey and Noble, 2008; Pieters and Noble, 2016; Noble et al., 2007), whereas these grains and others in the disordered rim of the ilmenite are shaped very differently. Ilmenite itself is opaque in the wavelength range of interest, but orientation effects in other phases could also affect npFe^0 shapes under certain conditions. While the influence of these non-spherical inclusions on optical measurements could be averaged out in bulk samples of randomly oriented grains (Pollack and Cuzzi, 1980) or adequately modeled by spheres of equivalent volume (Kelly et al., 2003), there are significant differences in the processes that can lead to the crack-filling inclusions here versus large spherical grains such as in agglutinates.

4.1.4. Surface orientation and exposure differences

In addition to the crystallographically aligned defects present in each region of the ilmenite, the orientation of the ilmenite lattice relative to the exposed surface also controls the maximum density of helium in the near-surface bubbles. Regions A and C are closely related spatially, and it is likely they experienced very similar exposure histories. However, the internal pressure of helium in bubbles in region C extend to much higher values than those in region A. Region D, oriented similarly to C, reaches comparably high pressure within the bubbles. The maximum internal

bubble pressure within a crystal depends on bubble radius r and surface tension γ of the crystal, $P \sim 2\gamma/r$. Regions A and B have surfaces nominally parallel to the $\{10\bar{1}1\}$ or $\{10\bar{1}0\}$ faces in ilmenite, which after $\{0001\}$ are at a minimum for surface energy for hcp crystals and thus at a minimum for possible pressure. In the $\{h0\bar{h}1\}$ family, relative surface energy reaches a maximum $\sim 35^\circ$ from $\{0001\}$, which is near the orientation of the exposed surfaces in C and some of D (Matysina, 1999). The alignment of the elongate npFe^0 in these regions, not generally noted in other space weathered materials, also indicates significant crystallographic effects and a possible relationship between vesicle formation and npFe^0 growth.

The general characteristics of the ilmenite space weathered rim are similar to those observed by Christoffersen et al. (1996), but the multiple exposed surfaces in this sample show a progression of exposure effects as well as the role of crystallographic orientation. Of the four regions delineated here, B appears to be the freshest surface with the least exposure to the solar wind. Compared to region A, which has a similar crystallographic relationship between the surface and the basal plane, B lacks large vesicles in the outer layer, has portions with little to no disordered outer layer, and generally has a smaller defect density in the inner layer. It is possible that portions of the B surface have experienced relatively recent exfoliation and resurfacing from processes that formed the long crack and Fe^0 grains in Fig. 4.

4.2. Helium trapping

A number of studies have looked at the amount of helium and other noble gases in lunar soils, both in bulk and at the grain-scale (Wieler, 2002 and references therein), quite a few of which have included soil 71501, both for ease of comparison between methods and because it is known to be relatively gas-rich compared to other sub-mature soils (e.g., Becker and Pepin, 1989; Benkert et al., 1993; Nichols et al., 1994). Both step-wise etching and heating have shown pulses of gas from very near the surface of the grains, which is consistent with implantation by the solar wind, as are the isotope ratios determined for the very-near-surface released gases (Heber et al., 2003). Ablation depth profiles of individual ilmenite grains also show a peak in helium that varies somewhat between soils and between grains, but is near 20 nm (Kirsten, 1977), consistent with estimates of implantation depth of solar wind helium from modelling of interaction of ions with matter (Christoffersen et al., 1996) and with vesicle depths measured here (Fig. 8; Supplementary Material S4). The total gas released from some individual grains in the heating and etching experiments is near the saturation limit for helium in ilmenite (Nichols et al., 1994), but it is unclear which, if any, of the natural ilmenites measured contained bubbles. Within a soil, the helium content of individual ilmenite grains can vary by up to a factor of ~ 20 (Nier and Schlutter, 1994), although saturation fluence of solar wind helium is reached in a few hundred years (Nichols et al., 1994).

Crushing experiments done on lunar soils release almost as much helium as heating and etching experiments (Funkhouser et al., 1971), indicating that a significant fraction of the helium is contained in bubbles or other cavities where it is easily released, rather than remaining as isolated interstitials. Using images to calculate vesicle volume and grain surface area in region A, and assuming $n_{\text{H}}/\text{cm}^3 = 40$, the maximum for the region, we estimate that large vesicles contain only 6–12% of the helium required to reach saturation concentration (Nichols et al., 1994). Estimates for the other regions return similar proportions of helium trapped in observable vesicles. Thus, if most helium is not present as interstitial atoms in the lattice, a significant amount of helium must remain in small defects and cavities 1–2 nm wide such as those highlighted in Fig. 6. Fig. 10 shows high magnification STEM images of the aligned defects in ilmenite along with schematic representations of the defects. HAADF images, which are sensitive to density, show the Fe and Ti atomic columns. The planar defects are dark lines ~ 1.4 nm wide (one unit cell in ilmenite). The defects appear dark because the helium-filled cavities are much less dense than the surrounding ilmenite.

The space weathered morphology and trapping of helium observed in the ilmenite and chromite are due both to the immediate material response to ion irradiation and the movement of atoms over significant periods of time. The implanted helium ions create a series of vacancies and interstitials along their path through the ilmenite before coming to a stop. Some proportion of the vacancies and interstitials recombine, and the helium atoms coalesce as part of dislocation loop-cavity complexes (Zinkle, 2012). Not all loops will be large enough to be observed easily in the TEM. Continued migration and condensation of point defects into extended defects reduce the elastic strain energy in the surrounding material, allowing crystallinity to be maintained to higher doses and driving the formation of vesicles (Wilson, 1987; Hobbs et al., 1994). The relationship between the energy shift of the signal and the helium density calculated from the signal intensity (Fig. 9a) is similar to that calculated for laboratory irradiated materials (Fréchal et al., 2009; Taverna et al., 2008), indicating that bubble formation and nucleation mechanisms are similar for natural and laboratory samples.

The evidence for heating in this sample is mixed. Previous observations of space weathered lunar ilmenites identified aligned planar defects but not larger vesicles (Christoffersen et al., 1996), so it is possible this grain experienced some amount of post-irradiation heating to induce their growth. The defect morphology observed in this grain compares well with experimentally irradiated alumina and spinel (structurally related to ilmenite and chromite, respectively) that were irradiated at 650°C , while an alumina sample irradiated at room temperature lacks crystallographically aligned defects (Zinkle, 2012). Thus, heating events could be required to form those textures at the lunar surface also. While the lack of rim and solar flare tracks in the silicate portions of the sample could indicate a small degree of exposure, as described above, they could also be due to loss of those features through annealing.

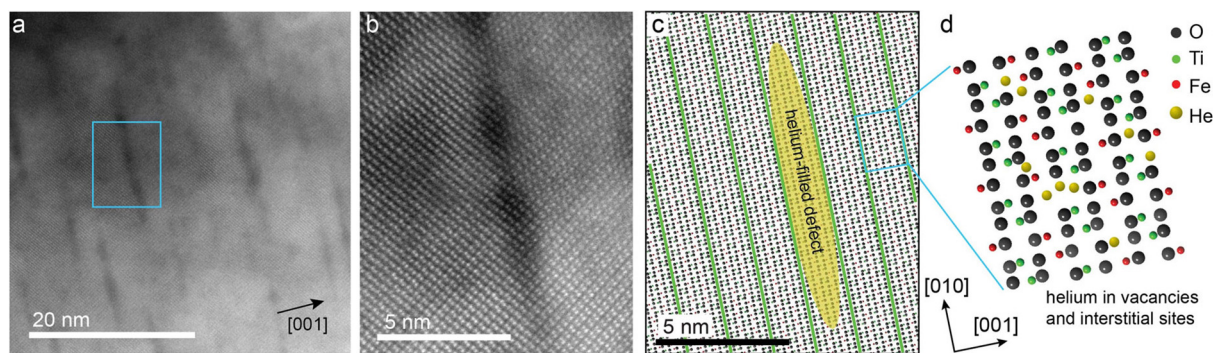


Fig. 10. (a) HAADF image of ilmenite with helium-filled aligned planar defects (section 1). Defects are dark due to low density of helium or empty cavity. (b) Atomic resolution HAADF image of planar defect and Fe and Ti atom columns. The defect is not the full thickness of the section, so structure is observed through the defect. (c) Schematic illustration of planar defect one unit cell wide and aligned with ilmenite basal plane, represented by the green lines. (d) Helium atoms are also present in the ilmenite as point defects in vacancies and interstitial sites.

Other evidence suggests that the sample did not experience significant heating. A layer of vesicles was seen in experimentally irradiated ilmenite that was not annealed (Christoffersen et al., 2010), providing evidence that heating may not be required for bubble nucleation in ilmenite. The close spatial association of bubbles in the ilmenite with very different interior pressures, as in Fig. 9b, suggests that bubble pressures are not at equilibrium. Similarly, the bubbles in this sample do not show a clear correlation between helium density and bubble size, unlike similar measurements of helium bubbles in metallic alloys that have been heated or annealed (Taverna et al., 2008; Walsh et al., 2000). The only other report on helium nano-bubbles in natural material, which was not intentionally annealed, also did not see any correlation between size and internal pressure (Seydoux-Guillaume et al., 2016). Additionally, the chromite, which does contain trapped helium, did not form vesicles, although spinel has been shown to do so when irradiated at high temperature with He and H together (Zinkle, 2012).

4.3. Solar wind irradiation throughout the solar system

There are significant differences in how space weathering affects materials in different parts of the Solar System, with lunar-type alteration forming the basis for much of our knowledge of the various processes (Pieters and Noble, 2016). However, the processes or mechanisms affecting the various bodies are not occurring in the same proportions or the same way everywhere. Samples from Itokawa, where space weathering is hypothesized to be much more strongly influenced by solar wind irradiation relative to impacts compared to on the Moon, have amorphous or nanocrystalline rims, some of which contain vesicles or npFe^0 or np-sulfide inclusions (Harries and Langenhorst, 2014; Matsumoto et al., 2015; Noguchi et al., 2014, 2011; Thompson et al., 2014). The Itokawa grain rims, both irradiated and vapor deposited, are generally much thinner than those observed on lunar soil grains. Micrometeorites and IDPs, which may experience a range of solar wind irradiation conditions, can show large ranges in noble gas abundances, elemental and isotopic ratios, and thermal

gas loss (Wieler, 2002 and references therein). Brownlee et al. (1998) observed euhedral cavities in IDP pyrrhotite, which is known to be very retentive of helium. They suggest that the euhedral shape, similar to some experimentally irradiated and annealed samples, is due to heating during atmospheric entry, which also allowed the bubbles to grow to observable dimensions.

Future observations of intra-grain heterogeneity in helium distribution and other weathering features in samples from other Solar System bodies, as seen in the lunar grain here, could also aid understanding of exposure time on those bodies, and whether particles were exposed to irradiation before or after agglomeration or ejection from a parent body. Relating bubble morphology to other characteristics of a sample, such as thermal or aqueous alteration features, could constrain when hydrogen or helium implantation occurred. Vesicles in a pyroxene IDP grain and in irradiated samples have been shown to contain spectroscopic signatures related to the presence of H/OH/water (Bradley et al., 2014), indicating, together with the present results, that EELS measurements could be used to identify a number of volatiles contributing to the formation of vesicles. The sensitivity of the technique to specific gasses depends on the details of the plasmon shape of the host material.

5. CONCLUSIONS

Silicate glass, chromite, and ilmenite exhibit distinct responses to space weathering when exposed along the surface of a single grain lunar soil grain, where they must have experienced the same weathering conditions. The three phases here show variations in rim thicknesses, coating composition, size, shape and areal density of npFe^0 inclusions, and defect and vesicle density. Were these phases in separate grains, these differences might be attributable to differences in the length of exposure time or to heating from nearby impacts, but in this single soil particle where the exposures are adjacent, the differences are clearly due only to material properties. Future attempts to relate absolute exposure ages to optical maturity and other parameters or to determine relative exposure ages between different airless

bodies will need to take into account the very different apparent weathering rates in different phases and how possible heating events could change the apparent ages in natural samples. The combination of measurements of helium density in bubbles with other estimates of exposure ages, such as detailed searches for solar flare tracks (Berger and Keller, 2015), could provide additional information about regolith processes and timing or duration of heating events. Additional STEM-EELS studies of multiphase grains in higher maturity lunar soils are needed to establish any quantitative relationship between solar flare track density and He vesicle formation features.

ACKNOWLEDGEMENTS

We thank CAPTEM and the curatorial staff at Johnson Space Center for providing access to the pristine lunar samples. This work was supported by the RIS⁴E node of NASA's Solar System Exploration Research Virtual Institute (SSERVI). This is manuscript SSERVI-2017-057. This manuscript has been improved through the constructive reviews of J. Bradley and two anonymous referees.

APPENDIX A. SUPPLEMENTARY MATERIAL

Supplementary data associated with this article can be found, in the online version, at <https://doi.org/10.1016/j.gca.2017.12.023>.

REFERENCES

- Arvidson R., Drozd R., Guinness E., Hohenberg C., Morgan C., Morrison R. and Oberbeck V. (1976) Cosmic ray exposure ages of Apollo 17 samples and the age of Tycho. *Lunar Planet. Sci. Conf.* **7**, 2817–2832.
- Becker R. H. and Pepin R. O. (1989) Long-term changes in solar wind elemental and isotopic ratios: a comparison of two lunar ilmenites of different antiquities. *Geochim. Cosmochim. Acta* **53**, 1135–1146. [https://doi.org/10.1016/0016-7037\(89\)90219-6](https://doi.org/10.1016/0016-7037(89)90219-6).
- Benkert J. P., Baur H., Signer P. and Wieler R. (1993) He, Ne, and Ar from the solar wind and solar energetic particles in lunar ilmenites and pyroxenes. *J. Geophys. Res.* **98**, 13147–13162. <https://doi.org/10.1029/93JE01460>.
- Bennett C. J., Pirim C. and Orlando T. M. (2013) Space-weathering of solar system bodies: a laboratory perspective. *Chem. Rev.* **113**, 9086–9150. <https://doi.org/10.1021/cr400153k>.
- Berg S. and Katardjiev I. V. (1999) Preferential sputtering effects in thin film processing. *J. Vac. Sci. Tech. A* **17**, 1916–1925. <https://doi.org/10.1116/1.581704>.
- Berger E. L. and Keller L. P. (2015) Solar flare track exposure ages in regolith particles: A calibration for transmission electron microscope measurements. *Lunar Planet. Sci. Conf.* **46**, #1543.
- Bernatowicz T., Nichols, Jr., R. and Hohenberg C. (1994) Origin of amorphous rims on lunar soil grains. *Lunar Planet. Sci. Conf.* **25**, 105.
- Borg J., Comstock G. M., Langevin Y., Maurette M., Jouffrey B. and Jouret C. (1976) A Monte Carlo model for the exposure history of lunar dust grains in the ancient solar wind. *Earth Planet. Sci. Lett.* **29**, 161–174. [https://doi.org/10.1016/0012-821X\(76\)90036-4](https://doi.org/10.1016/0012-821X(76)90036-4).
- Bradley J. P., Ishii H. A., Gillis-Davis J. J., Ciston J., Nielsen M. H., Bechtel H. A. and Martin M. C. (2014) Detection of solar wind-produced water in irradiated rims on silicate minerals. *Proc. Nat. Acad. Sci.* **111**, 1732–1735. <https://doi.org/10.1073/pnas.1320115111>.
- Brownlee D., Joswiak D., Bradley J., Schlutter D. and Pepin R. (1998) Tiny bubbles: Direct observation of He in IDPs. *Lunar Planet. Sci. Conf.* **29**, #1869.
- Carrez P., Demyk K., Cordier P., Gengembre L., Grimblot J., D'Hendecourt L., Jones A. P. and Leroux H. (2002) Low-energy helium ion irradiation-induced amorphization and chemical changes in olivine: insights for silicate dust evolution in the interstellar medium. *Meteor. Planet. Sci.* **37**, 1599–1614. <https://doi.org/10.1111/j.1945-5100.2002.tb00814.x>.
- Carter G. and Nobes M. J. (2011) A phenomenological model of ion-induced crystallization and amorphization. *J. Mater. Res.* **6**, 2103–2108. <https://doi.org/10.1557/JMR.1991.2103>.
- Christoffersen R., Keller L., Rahman Z. and Baragiola R. (2010) Experimental investigation of space radiation processing in lunar soil ilmenite: Combining perspectives from surface science and transmission electron microscopy. *Lunar Planet. Sci. Conf.* **41**, #1532.
- Christoffersen R. and Keller L. P. (2011) Space radiation processing of sulfides and silicates in primitive solar systems materials: comparative insights from in situ TEM ion irradiation experiments. *Meteor. Planet. Sci.* **46**, 950–969. <https://doi.org/10.1111/j.1945-5100.2011.01203.x>.
- Christoffersen R., McKay D. S. and Keller L. P. (1996) Microstructure, chemistry, and origin of grain rims on ilmenite from the lunar soil finest fraction. *Meteor. Planet. Sci.* **31**, 835–848. <https://doi.org/10.1111/j.1945-5100.1996.tb02117.x>.
- David M.-L., Alix K., Pailloux F., Mauchamp V., Couillard M., Botton G. A. and Pizzagalli L. (2014) In situ controlled modification of the helium density in single helium-filled nanobubbles. *J. Appl. Phys.* **115**, 123508. <https://doi.org/10.1063/1.4869213>.
- Egerton R. F. (2011) *Electron Energy-Loss Spectroscopy in the Electron Microscope*, third ed. Springer, New York.
- Fréchal S., Walls M., Kociak M., Chevalier J. P., Henry J. and Gorse D. (2009) Study by EELS of helium bubbles in a martensitic steel. *J. Nucl. Mat.* **393**, 102–107. <https://doi.org/10.1016/j.jnucmat.2009.05.011>.
- Funkhouser J., Jessberger E., Müller O. and Zähringer J. (1971) Active and inert gases in Apollo 12 and Apollo 11 samples released by crushing at room temperature and by heating at low temperatures. *Lunar Planet. Sci. Conf.* **2**, 1381–1396.
- Glotch T. D., Bandfield J. L., Lucey P. G., Hayne P. O., Greenhagen B. T., Arnold J. A., Ghent R. R. and Paige D. A. (2015) Formation of lunar swirls by magnetic field standoff of the solar wind. *Nat. Commun.* **6**, 6189. <https://doi.org/10.1038/ncomms7189>.
- Hapke B. (2001) Space weathering from Mercury to the asteroid belt. *J. Geophys. Res.* **106**, 10039–10073. <https://doi.org/10.1029/2000JE001338>.
- Harries D. and Langenhorst F. (2014) The mineralogy and space weathering of a regolith grain from 25143 Itokawa and the possibility of annealed solar wind damage. *Earth Planet. Space* **66**, 1–11. <https://doi.org/10.1186/1880-5981-66-118>.
- Heber V. S., Baur H. and Wieler R. (2003) Helium in lunar samples analyzed by high-resolution stepwise etching: implications for the temporal constancy of solar wind isotopic composition. *Astrophys. J.* **597**, 602–614. <https://doi.org/10.1086/378402>.
- Heck P. R., Schmitz B., Baur H., Halliday A. N. and Wieler R. (2004) Fast delivery of meteorites to Earth after a major asteroid collision. *Nature* **430**, 323–325. <https://doi.org/10.1038/nature02736>.

- Heck P. R., Marhas K. K., Hoppe P., Gallino R., Baur H. and Wieler R. (2007) Presolar He and Ne isotopes in single circumstellar SiC grains. *Astrophys. J.* **656**, 1208. <https://doi.org/10.1086/510478>.
- Hemingway D. J., Garrick-Bethell I. and Kreslavsky M. A. (2015) Latitudinal variation in spectral properties of the lunar maria and implications for space weathering. *Icarus* **261**, 66–79. <https://doi.org/10.1016/j.icarus.2015.08.004>.
- Hobbs L. W., Clinard F. W., Zinkle S. J. and Ewing R. C. (1994) Radiation effects in ceramics. *J. Nucl. Mat.* **216**, 291–321. [https://doi.org/10.1016/0022-3115\(94\)90017-5](https://doi.org/10.1016/0022-3115(94)90017-5).
- Jäger W., Mancke R., Trinkaus H., Crecelius G., Zeller R., Fink J. and Bay H. L. (1982) Density and pressure of helium in small bubbles in metals. *J. Nucl. Mat.* **111–112**, 674–680. [https://doi.org/10.1016/0022-3115\(82\)90288-4](https://doi.org/10.1016/0022-3115(82)90288-4).
- Kehm K., Flynn G. J., Sutton S. R. and Hohenberg C. M. (2002) Combined noble gas and trace element measurements on individual stratospheric interplanetary dust particles. *Meteor. Planet. Sci.* **37**, 1323–1335. <https://doi.org/10.1111/j.1945-5100.2002.tb01031.x>.
- Keilm S. and Langseth, Jr, M. (1973) Surface brightness temperatures at the Apollo 17 heat flow site: thermal conductivity of the upper 15 cm of regolith. *Lunar Planet. Sci. Conf.* **4**, 2503–2513.
- Keller L., Christoffersen R. and McKay D. (1995) The oxidation state of altered rims on ilmenite from lunar soils. *Lunar Planet. Sci. Conf.* **26**, 729.
- Keller L. P. and McKay D. S. (1993) Discovery of vapor deposits in the lunar regolith. *Science* **261**, 1305–1307. <https://doi.org/10.1126/science.261.5126.1305>.
- Keller L. P. and McKay D. S. (1997) The nature and origin of rims on lunar soil grains. *Geochim. Cosmochim. Acta* **61**, 2331–2341. [https://doi.org/10.1016/S0016-7037\(97\)00085-9](https://doi.org/10.1016/S0016-7037(97)00085-9).
- Kelly K. L., Coronado E., Zhao L. L. and Schatz G. C. (2003) The optical properties of metal nanoparticles: the influence of size, shape, and dielectric environment. *J. Phys. Chem. B* **107**, 668–677. <https://doi.org/10.1021/jp026731y>.
- Kirsten T. (1977) Rare gases implanted in lunar fines. *Philos. Trans. Roy. Soc. Lond. Ser. A* **285**, 391–395. <https://doi.org/10.1098/rsta.1977.0079>.
- Lucey P. G. and Noble S. K. (2008) Experimental test of a radiative transfer model of the optical effects of space weathering. *Icarus* **197**, 348–353. <https://doi.org/10.1016/j.icarus.2008.05.008>.
- Matsumoto T., Tsuchiyama A., Miyake A., Noguchi T., Nakamura M., Uesugi K., Takeuchi A., Suzuki Y. and Nakano T. (2015) Surface and internal structures of a space-weathered rim of an Itokawa regolith particle. *Icarus* **257**, 230–238. <https://doi.org/10.1016/j.icarus.2015.05.001>.
- Matsumoto T., Tsuchiyama A., Uesugi K., Nakano T., Uesugi M., Matsuno J., Nagano T., Shimada A., Takeuchi A., Suzuki Y., Nakamura T., Nakamura M., Gucsik A., Nagaki K., Sakaiya T. and Kondo T. (2016) Nanomorphology of Itokawa regolith particles: application to space-weathering processes affecting the Itokawa asteroid. *Geochim. Cosmochim. Acta* **187**, 195–217. <https://doi.org/10.1016/j.gca.2016.05.011>.
- Matysina Z. (1999) The relative surface energy of hexagonal close-packed crystals. *Mater. Chem. Phys.* **60**, 70–78. [https://doi.org/10.1016/S0254-0584\(99\)00050-4](https://doi.org/10.1016/S0254-0584(99)00050-4).
- Merrihue C. (1964) Rare gas evidence for cosmic dust in modern pacific red clay. *Ann. NY Acad. Sci.* **119**, 351–367. <https://doi.org/10.1111/j.1749-6632.1965.tb47445.x>.
- Nichols R., Hohenberg C. and Olinger C. (1994) Implanted solar helium, neon, and argon in individual lunar ilmenite grains: surface effects and a temporal variation in the solar wind composition. *Geochim. Cosmochim. Acta* **58**, 1031–1042. [https://doi.org/10.1016/0016-7037\(94\)90524-X](https://doi.org/10.1016/0016-7037(94)90524-X).
- Nier A. O. and Schlutter D. J. (1992) Extraction of helium from individual interplanetary dust particles by step-heating. *Meteoritics* **27**, 166–173. <https://doi.org/10.1111/j.1945-5100.1992.tb00744.x>.
- Nier A. and Schlutter D. (1994) Helium and neon in lunar ilmenites of different antiquities. *Meteoritics* **29**, 662–673. <https://doi.org/10.1111/j.1945-5100.1994.tb00782.x>.
- Noble S. K., Keller L. P. and Pieters C. M. (2005) Evidence of space weathering in regolith breccias I: lunar regolith breccias. *Meteor. Planet. Sci.* **40**, 397–408. <https://doi.org/10.1111/j.1945-5100.2005.tb00390.x>.
- Noble S. K., Pieters C. M. and Keller L. P. (2007) An experimental approach to understanding the optical effects of space weathering. *Icarus* **192**, 629–642. <https://doi.org/10.1016/j.icarus.2007.07.021>.
- Noguchi T., Nakamura T., Kimura M., Zolensky M. E., Tanaka M., Hashimoto T., Konno M., Nakato A., Ogami T., Fujimura A., Abe M., Yada T., Mukai T., Ueno M., Okada T., Shirai K., Ishibashi Y. and Okazaki R. (2011) Incipient space weathering observed on the surface of Itokawa dust particles. *Science* **333**, 1121–1125. <https://doi.org/10.1126/science.1207794>.
- Noguchi T., Kimura M., Hashimoto T., Konno M., Nakamura T., Zolensky M. E., Okazaki R., Tanaka M., Tsuchiyama A., Nakato A., Ogami T., Ishida H., Sagae R., Tsuchimoto S., Matsumoto T., Matsuno J., Fujimura A., Abe M., Yada T., Mukai T., Ueno M., Okada T., Shirai K. and Ishibashi Y. (2014) Space weathered rims found on the surfaces of the Itokawa dust particles. *Meteor. Planet. Sci.* **49**, 188–214. <https://doi.org/10.1111/maps.12111>.
- Pepin R., Becker R. and Schlutter D. (1999) Irradiation records in regolith materials. I: Isotopic compositions of solar-wind neon and argon in single lunar mineral grains. *Geochim. Cosmochim. Acta* **63**, 2145–2162. [https://doi.org/10.1016/S0016-7037\(99\)00002-2](https://doi.org/10.1016/S0016-7037(99)00002-2).
- Pepin R. O., Palma R. L., Gehr R. D. and Starrfield S. (2011) Presolar grains from novae: evidence from neon and helium isotopes in comet dust collections. *Astrophys. J.* **742**, 86. <https://doi.org/10.1088/0004-637X/742/2/86>.
- Pieters C. M. and Noble S. K. (2016) Space weathering on airless bodies. *J. Geophys. Res.* **121**, 1865–1884. <https://doi.org/10.1002/2016JE005128>.
- Pieters C. M., Taylor L. A., Noble S. K., Keller L. P., Hapke B., Morris R. V., Allen C. C., McKay D. S. and Wentworth S. (2000) Space weathering on airless bodies: resolving a mystery with lunar samples. *Meteor. Planet. Sci.* **35**, 1101–1107. <https://doi.org/10.1111/j.1945-5100.2000.tb01496.x>.
- Pollack J. B. and Cuzzi J. N. (1980) Scattering by nonspherical particles of size comparable to a wavelength: a new semi-empirical theory and its application to tropospheric aerosols. *J. Atmos. Sci.* **37**, 868–881. [https://doi.org/10.1175/1520-0469\(1980\)037<0868:SBNPOS>2.0.CO;2](https://doi.org/10.1175/1520-0469(1980)037<0868:SBNPOS>2.0.CO;2).
- Rajan R. S., Brownlee D. E., Tomandl D., Hodge P. W., Farrar H. and Britten R. A. (1977) Detection of ^4He in stratospheric particles gives evidence of extraterrestrial origin. *Nature* **267**, 133–134. <https://doi.org/10.1038/267133a0>.
- Rice P. M. and Zinkle S. J. (1998) Temperature dependence of the radiation damage microstructure in V-4Cr-4Ti neutron irradiated to low dose. *J. Nucl. Mat.* **258**, 1414–1419. [https://doi.org/10.1016/S0022-3115\(98\)00208-6](https://doi.org/10.1016/S0022-3115(98)00208-6).
- Sasaki S., Nakamura K., Hamabe Y., Kurahashi E. and Hiroi T. (2001) Production of iron nanoparticles by laser irradiation in a simulation of lunar-like space weathering. *Nature* **410**, 555–557. <https://doi.org/10.1038/35069013>.
- Seydoux-Guillaume A.-M., David M.-L., Alix K., Datas L. and Bingen B. (2016) Trapping of helium in nano-bubbles in

- euxenite: positive identification and implications. *Earth Planet. Sci. Lett.* **448**, 133–139. <https://doi.org/10.1016/j.epsl.2016.05.013>.
- Signer P., Baur H., Derksen U., Etique P., Funk H., Horn P. and Wieler R. (1977) Helium, neon, and argon records of lunar soil evolution. *Lunar Planet. Sci. Conf.* **8**, 3657–3683.
- Suess H. E., Wänke H. and Wlotzka F. (1964) On the origin of gas-rich meteorites. *Geochim. Cosmochim. Acta* **28**, 595–607. [https://doi.org/10.1016/0016-7037\(64\)90080-8](https://doi.org/10.1016/0016-7037(64)90080-8).
- Taverna D., Kociak M., Stéphan O., Fabre A., Finot E., Décamps B. and Colliex C. (2008) Probing physical properties of confined fluids within individual nanobubbles. *Phys. Rev. Lett.* **100**, 035301. <https://doi.org/10.1103/PhysRevLett.100.035301>.
- Taylor L. A., Pieters C. M., Keller L. P., Morris R. V. and McKay D. S. (2001) Lunar mare soils: space weathering and the major effects of surface-correlated nanophase Fe. *J. Geophys. Res.* **106**, 27985–27999. <https://doi.org/10.1029/2000JE001402>.
- Thompson M. S., Christoffersen R., Zega T. J. and Keller L. P. (2014) Microchemical and structural evidence for space weathering in soils from asteroid Itokawa. *Earth Planet. Space* **66**, 89. <https://doi.org/10.1186/1880-5981-66-89>.
- Thompson M. S., Zega T. J., Becerra P., Keane J. T. and Byrne S. (2016) The oxidation state of nanophase Fe particles in lunar soil: implications for space weathering. *Meteor. Planet. Sci.* **51**, 1082–1095. <https://doi.org/10.1111/maps.12646>.
- Walsh C. A., Yuan J. and Brown L. M. (2000) A procedure for measuring the helium density and pressure in nanometre-sized bubbles in irradiated materials using electron-energy-loss spectroscopy. *Philos. Mag. A* **80**, 1507–1543. <https://doi.org/10.1080/01418610008212134>.
- Wieler R. (2002) Noble gases in the solar system. *Rev. Mineral. Geochem.* **47**, 21–70. <https://doi.org/10.2138/rmg.2002.47.2>.
- Wieler R., Etique P., Signer P. and Poupeau G. (1980) Record of the solar corpuscular radiation in minerals from lunar soils—A comparative study of noble gases and tracks. *Lunar Planet. Sci. Conf.* **11**, 1369–1393.
- Wilson I. H. (1987) Synthesis of dielectric layers in silicon by ion implantation. In *Ion Beam Modification of Insulators* (eds. P. Mazzoldi and G. W. Arnold). Elsevier, Netherlands, pp. 245–300.
- Zhang S. and Keller L. (2010) A STEM-EELS study of the effect of solar-wind irradiation on the ilmenite from lunar soil. *Microsc. Microanal.* **16**, 1216–1217. <https://doi.org/10.1017/S1431927610057053>.
- Zhang S. and Keller L. P. (2011) Space weathering effects in lunar soils: the roles of surface exposure time and bulk chemical composition. *Lunar Planet. Sci. Conf.* **42**, #1947.
- Zinkle S. J. (2012) Effect of H and He irradiation on cavity formation and blistering in ceramics. *Nucl. Inst. Meth. Phys. Res. B* **286**, 4–19. <https://doi.org/10.1016/j.nimb.2012.03.030>.

Associate Editor: Pierre Beck